Real-Time Phosphate Monitoring via Plant-derived Graphene Ink FET Sensors Integrated with Deep Learning

Rapti Ghosh,[1,2] Fengxue Zhang,[3] Hyun-June Jang,[1,2] Janan Hui,[4] Kayla Vittore,[5] Haoyang You,[6] Rozyyev Vepa,[7] Wen Zhuang,[1,2] Xingkang Huang,[1,2] Haihui Pu,[1,2] Jeffrey W. Elam,[7] Stuart J. Rowan,[1,2,6] DoKyoung Lee,[5] Elizabeth A. Ainsworth,[5,8] Mark C. Hersam,[4,9] Yuxin Chen,[3] Junhong Chen[1,2]*

[1] Pritzker School of Molecular Engineering, University of Chicago, Chicago, IL 60637, USA

[2] Chemical Sciences and Engineering Division, Physical Sciences and Engineering Directorate, Argonne National Laboratory, Lemont, IL 60439, USA

[3] Department of Computer Science, University of Chicago, Chicago, IL 60637, USA

[4] Department of Chemistry, Northwestern University, Evanston, Illinois 60208, USA

[5] Department of Crop Sciences, University of Illinois Urbana−Champaign, Urbana, Illinois 61801, USA

[6] Department of Chemistry, University of Chicago, Chicago, Illinois 60637 United States

[7] Applied Materials Division, Argonne National Laboratory, Lemont, IL, 60439, USA

[8] Department of Plant Biology, University of Illinois Urbana Champaign, Urbana, Illinois 61801, USA

9 Department of Materials Science and Engineering, Northwestern University, Evanston, Illinois 60208, USA

*Corresponding author: Junhong Chen: junhongchen@uchicago.edu

Abstract: Real-time monitoring of plant nutrient levels, particularly phosphate, is essential for optimizing plant growth and addressing nutrient imbalances in precision agriculture. Conventional sensors mostly suffer from poor stability, reproducibility, matrix effects, and high costs, limiting their scalability and practical application. To overcome these challenges, a deep learning (DL)-integrated remote-gate field-effect transistor (FET) sensor utilizing a plant-derived graphene electrode is introduced for enhanced performance and reliability. These solution-processed graphene electrodes, composed of cellulose nanocrystals (CNCs) from plant fibers, are functionalized with phosphate-capturing ferritin and serve as the sensing surface, capacitively coupled to a commercial n-type FET to address device variability issues. DL integration significantly improved accuracy, enabling robust and precise phosphate detection. The sensor demonstrates a sensitivity of 14.1 mV/dec after the pH correction, a coefficient of variation (CV) of responses below 5%, and a 1 ng/mL (1 ppb) detection limit. As a proof-of-concept, phosphate levels in Hoagland solution, a standard plant nutrient medium, were monitored, achieving an r^2 of 0.951 and a CV of 5.39%. A handheld prototype system further demonstrates its potential for on-site continuous monitoring. This sustainable and cost-effective approach provides a scalable solution for real-time phosphate detection with high sensitivity and reproducibility, meeting agricultural demands.

Keywords: Phosphate ion sensing, Remote-gate FET, Graphene-based FET, Handheld prototype sensor, Deep learning

1. Introduction

Efficient monitoring of plant nutrient availability in growth media is critical for optimizing agricultural productivity and mitigating environmental risks. Excessive use of phosphorus and nitrogen-containing fertilizers has adverse ecological effects, including eutrophication, algal blooms, and hypoxic dead zone formation in water bodies.[1] These disruptions in aquatic ecosystems cause hypoxia area formation of up to 23,000 km^2 in the Gulf of Mexico and the Mississippi River Delta at mid-summer, highlighting the urgent need for precise nutrient management.[2, 3] While regulatory agencies like the Environmental Protection Agency (EPA) have attempted to reduce nutrient content in fertilizers, the lack of reliable real-time measurement tools makes balancing agricultural needs with ecological sustainability difficult.[4] [5]

Innovative approaches like the aeroponic system maximize nutrient use efficiency by suspending plants without soil and delivering nutrients as mist.[6] Maintaining nutrient concentrations and balance for both macro- and micronutrients in mist water is key to sustainable production systems. Among macronutrients, a phosphorus deficiency causes the discoloration of leaves and early death of seedlings. [7] The phosphorus concentrations in the nutrient solution must be balanced with the other nutrients (e.g., nitrogen, potassium) for optimal plant growth stages. As reported, leafy green vegetables require lower phosphorus uptake during their seedling stage, approximately 5-10 ppm. However, this uptake increases to 15-30 ppm during the vegetative stage to facilitate the development of a healthy rooting system.[8] Bioelectronics such as sensors and actuators can be specifically integrated with plants to monitor their growth parameters, vital nutrient consistency, temperature, and other physiological conditions.[9] However, conventional sensors often fail to solve the sensitivity and real-time needs of such applications.[10]

A plant tissue test is the most common method for diagnosing nutrient balance and deficiency. Conventional phosphate measurement methods like lab-based chemical analyses, involve plant tissue collection and shipment to specialized facilities.[11] This process often requires several days which impedes timely interventions, causing nutrient imbalances that reduce plant yields, inhibit plant growth, and increase production costs.[12] In precision agriculture, real-time monitoring of nutrient availability is vital for optimizing fertilizer use to meet plant nutrient requirements. Slow responses often lead to the overuse of fertilizers and contribute to waterway pollution. Traditional sensing technologies such as optical,[13] ion-selective,[14] and electrochemical sensors[15] frequently lack the sensitivity required to detect low phosphate levels critical for early deficiency diagnosis. Hence, the integration of new real-time and on-site sensor data with precise nutrient management systems is essential to minimize waste, enhance crop productivity, and improve sustainability.

Portable commercial phosphate sensors use reagents (e.g., Ammonium Molybdate) for detection and have limited sensitivity (>0.02 mg/L for Hach) and real-time monitoring capabilities, especially in turbid or colored water.[16] High-precision automated analyzers offer continuous measurements with low detection limits of 0.001 mg/L but are expensive and require regular expert maintenance. On the other hand, the affordable sensors have poor detection limits (~0.1 mg/L) and are prone to ion interference.[17] Sensitivity, reagent dependency, and high costs remain significant barriers to the available sensors that hinder scalable and real-time agricultural use.

Field-effect transistor (FET) sensors have emerged as a promising alternative for phosphate detection due to their simplicity, rapid response, and scalability. Examples include reduced graphene oxide- and ZnO nanorods-based FETs, which have been demonstrated for phosphate and multi-ion detection.[18] [19] However, traditional FET sensors often suffer from performance

inconsistencies caused by device-to-device variations and the degradation of their semiconducting layers when exposed to analyte solutions, making them unreliable for continuous monitoring and limiting their commercial application.[20] To address these limitations, a few studies have integrated deep learning (DL) analysis into the sensing systems, distinguishing it from traditional FET-based approaches. The DL analysis preprocesses the FET's transfer curves to calibrate device-to-device variability and correct experimental biases that typically undermine performance in low-dimensional systems. Furthermore, the DL method leverages the kinetic data extracted from the curves to identify latent signals for sensing calibration.[21] For instance, Zhang J. et al. demonstrated that DL analysis effectively identifies interferences in biosensor signals, improving accuracy in complex environments.[22] Similarly, Desale K. S. et al. highlighted the potential of DL models to identify and compensate for signal drift, a common challenge in FET-based systems.[23] Additionally, Babu, A.V. et al. emphasized the real-time data processing and adaptive calibration capabilities of DL analysis.[24]

In this study, by applying DL models, we significantly enhance the sensor's reliability and accuracy, achieving a robust r^2 value of 0.951 for phosphate detection. The proposed DL approach is novel because it leverages two parallel convolutional neural networks (CNNs).[25] The architecture allows the model to extract complementary latent features from both two-dimensional and one-dimensional kinetic data, which are fused to generate more accurate numerical predictions. Our innovative signal extraction strategy and model architecture enable the sensor to distinguish specific phosphate signals from non-specific environmental noises, a critical improvement over previous methods. To demonstrate the system's practicality, we tested it in an aeroponic cultivation setup to monitor phosphate concentrations in Hoagland fertilizer solutions.

In blind tests, the DL-enhanced sensor achieves a coefficient of variation (CV) of 5.4%, accurately monitoring phosphate levels across multiple devices.

To complement the DL method, we design a remote-floating-gate FET sensor using sustainable and scalable plant-derived graphene ink. This eco-friendly graphene ink is composed of exfoliated biochar from hardwood[26] and cellulose nanocrystals as a bio-renewable dispersant in water. The plant-based sourcing reduces the environmental impacts for the production of the FET sensor, with the potential to contribute to a circular economy for cellulosic waste.[27] [28] In this configuration, the graphene-ink-coated silicon wafer acts as a sensing surface and is capacitively coupled to the gate of a commercial n-type FET. This ensures that the 2D structure of the sensing surface is preserved and electrically isolated,[29] which prevents unwanted redox reactions and mitigates signal fluctuations caused by ion diffusion or gate current flow, improving stability and reproducibility. The graphene ink surface, functionalized with phosphate-specific molecular probe ferritin, enhances the sensor's selectivity and sensitivity, resulting in a Nernstian response of 18 mV/pH.[19] The sensor demonstrated a sensitivity of 14.1 mV/dec after the pH correction, with a limit of detection (LOD) of 1 ng/mL and a CV of responses below 5% across different concentrations ranging up to 5 mg/mL. For real-time monitoring purposes, a handheld device prototype was developed that continuously measures the phosphate concentration for over 100 minutes with high selectivity in a mixed ion environment. By integrating DL with plant-derived carbon materials in a remote-gate FET sensor, our approach provides a scalable and cost-effective solution for real-time nutrient monitoring in agriculture. This platform has the potential to improve nutrient management in sustainable hydroponic, aeroponic, and aquaponic systems.
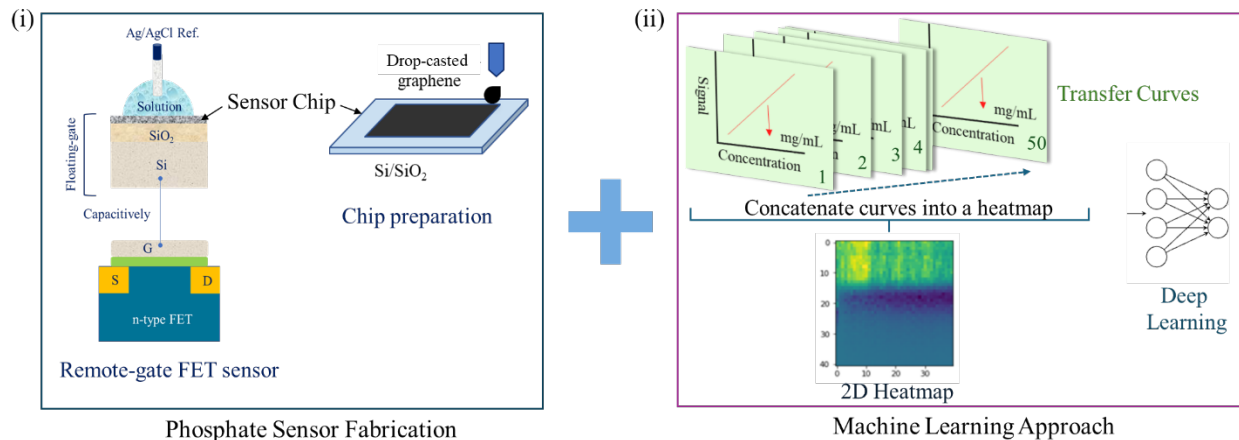
Figure. 1: Low-cost FET sensor fabrication using plant-based material to monitor phosphate concentration in plant growth solutions and integration of the FET sensor with machine learning. (i) Gate dependence study using a remote gate FET setup. The insulator electrically isolates the drop-casted plant-derived graphene layer and capacitively connected to the gate of the FET transducer while keeping the 2D structure of the film confined only to the analyte interface; (ii) Machine learning signal processing framework overview. The 50 cycles of the transfer curves measured in the remote gate setup are collectively converted into a 2D heatmap for the deep learning analysis.

2. Results and Discussion

This work aims to develop a scalable, low-cost, and recyclable sensor fabrication using nature-derived resources. The sensor design converges three domains: a) cellulose nanocrystals (CNCs) extraction from plants, b) plant-derived graphene ink synthesis, and c) sustainable production of sensor chips. As shown in Figure S1, CNCs are extracted from agricultural residues [Details in the experimental section] using standard chemical treatments.[27] The CNCs, which act as nanoscale surfactants/exfoliants, are dispersed in deionized water and plant-based graphite flakes are added. The mixture is sonicated and/or stirred to access graphene nanosheet/CNC dispersion via the liquid exfoliation method. This results in a well-consistent ink formulation which after filtration is deposited on a silicon wafer. After annealing at 600 °C (optimized temperature) and ferritin-probe functionalization the sensor chips are prepared for testing [Figure 1 (i) and S3]. Injecting 35 µL of phosphate solution onto the sensor's surface established the connection between

7

the chip and the gate terminal of an FET. As soon as the connection is established, a series of concentration-specific phosphate complexation reactions begin. This results in real-time surface charge modulation at the sensing surface, which was continuously recorded over 5 minutes as repeated transfer curves. These transfer curves are converted into 2D heatmaps retaining all the kinetic information related to a specific concentration [Figure 1 (ii)]. The DL analysis further probes the data to optimize the subset and quantify unknown samples' phosphate concentration. These sensors could be used to monitor phosphate levels in aeroponic plants, which are used to derive graphene ink, supporting a circular and sustainable bio-electronics manufacturing paradigm.
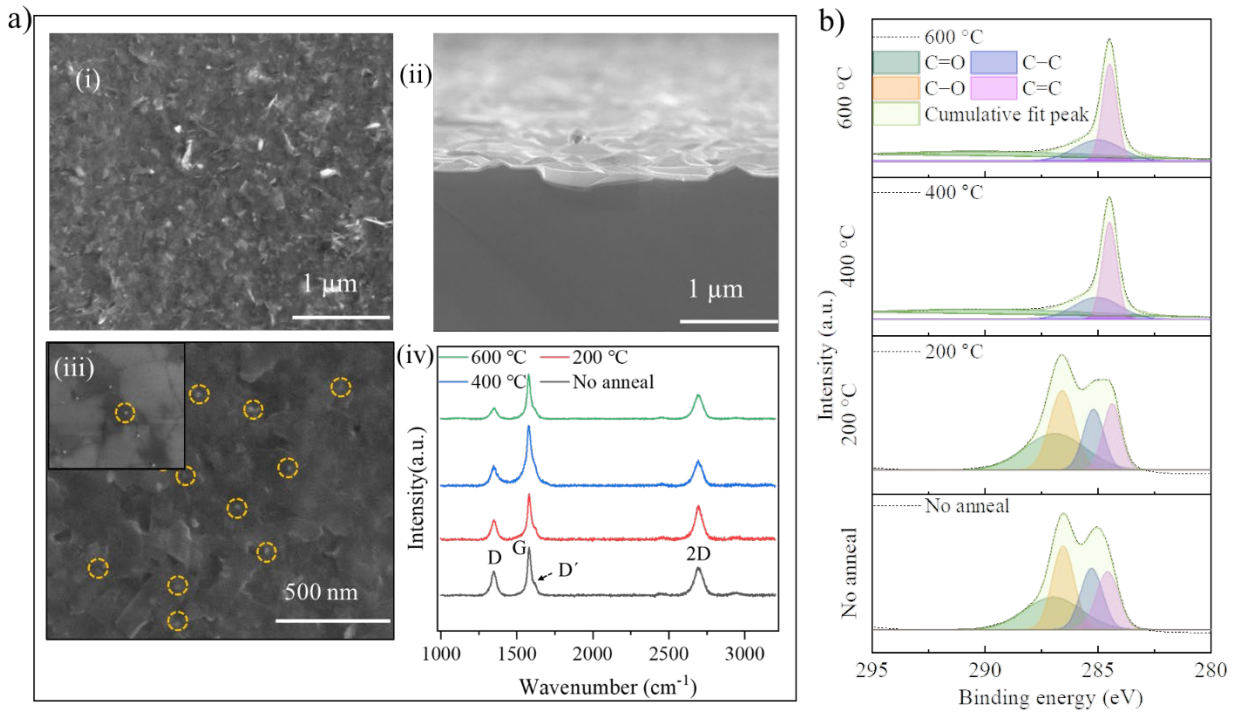

Figure. 2: a) (i) Top-view, (ii) Cross-sectional SEM image of bio-based graphene ink deposited on the Si/SiO$_2$ substrate, and (iii) Top-view SEM image of the ferritinized bio-based graphene ink sample, where the yellow circles indicate ferritin protein distribution on the film surface; (iv) Raman spectra and b) XPS spectra of the bio-based graphene ink sample annealed at different temperatures.

Thickness and uniformity are major factors in ink-based device fabrication. Figure 2a (i) and S2 showcase a uniform ink distribution on the Si/SiO$_2$ substrate. The scanning electron microscopy (SEM) (top-view) and atomic force microscopy (AFM, Figure S2) images confirm a multilayer graphene deposition without potential discontinuity. In the cross-sectional SEM image Figure 2a (ii), the thickness is around 0.9-1 µm. Apart from thickness optimization, the annealing process also removes/carbonizes the non-conductive CNCs which otherwise could adversely affect the device's performance. After the ink deposition on the substrate, the chips were annealed in a vacuum at 600 °C under the nitrogen flow at a 50 sccm rate for 30 minutes. From the analysis of Raman spectra in Figure 2a (iv), it can be concluded that with the increase of annealing temperature from no annealing condition to 600 °C the I$_D$/I$_G$ ratio decreased (Figure S3), which signifies the removal/carbonization of the CNCs with the increase of annealing temperature.[30] [31]Additionally, the intensity of the D′ band diminished with an eventual merging with the G band with the increase in temperature. Detailed analysis of I(D)/I(D′) $\cong$ 3 at lower annealing temperatures suggests the presence of sp^3 type of defects or charge impurities.[32] This appears because of the presence of the different oxygen-containing functional groups (e.g., –COOH, –OH) from the CNC in the ink during synthesis. With the increase in annealing temperature, these functional groups are removed, and only high-quality graphene or sp^2 carbon remains. This is supported by the X-ray photoelectron spectroscopy (XPS) spectra of the sample in Figure 2b, where it is observed that at lower annealing temperatures C=O and C–O peaks are prominent, consistent with the presence of the oxygen-containing functional groups on the graphene surface. With the increase in annealing temperature, these peaks diminish and the C=C peaks becomes the prominent peak with the increase/broadening of the C–C peak. This is consistent with higher annealing temperatures removing the oxygen-

containing species and reducing the amount of aliphatic carbon, resulting in mostly sp^2 graphitic carbon atoms in the film.[33]

After optimizing the annealing temperature, the 1-pyrenebutyric acid N-hydroxysuccinimide ester (PBASE) linker is attached to the film surface via pyrene-graphite interactions,[34] followed by the immobilization of the phosphate-sensitive ferritin protein molecule on the surface through NHS ester-amine coupling between PBASE and ferritin (Figure S1 and experimental section).[35] As shown in Figure 2a (iii), these hollow globular ferritin molecules are uniformly dispersed without aggregation. The functionalized chips were then exposed to phosphate solutions using a remote-gate FET platform, where the injection of phosphate solution caused a surface reaction altering the sensor's conductance.

When phosphate ions were introduced, a change in threshold voltage (ΔV_{Th}, see definition in the experimental section) was observed, with a monotonic increase from 1 pg/mL (1 ppt) to 5 mg/mL (5,000 ppm) (Figure 3a). This is due to the adsorption of phosphate ions (HPO_4^{2-}) by ferritin, inducing a negative gating effect on the n-type FET through a chemical interaction (Reaction 1) between ferritin's iron core and HPO_4^{2-} ions:[36] [19]

$$FeO–OH + HPO_4^{2-} \rightarrow FeO–(O)–PO_3^{2-} + H_2O \qquad ....Reaction\ 1$$
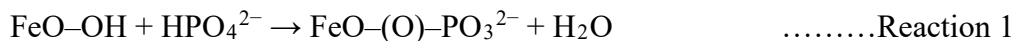
At concentrations below 1 ng/mL (1 ppb), the response was minimal but increased significantly above 1 ng/mL with a slope of 20.96 mV/dec, indicating a detectable range of 1 ng/mL to 3 mg/mL (blue curve, Figure 3a). pH effects, varying from 5.9 (at lower concentrations) to 8.1 (at higher concentrations), were observed to influence V_{Th}, following a Nernstian response of 18 mV/pH with an r^2 of 0.998 (Figure S4). A control experiment with a non-ferritinized bio-based graphene device showed a nearly linear response across concentrations (Red curve, Figure

3a) with a slope value of 6.86 mV/dec, likely due to the pH change. This confirms that the phosphate-induced conductance change prevails over the pH effects in the ferritinized sample. Subtracting this pH influence yielded a sensitivity of 14.1 mV/dec (Calculations detailed in the supporting information) for the ferritinized bio-based graphene device.

Across all devices, the response was consistent (CV < 5%), indicating reliability for practical use (Figure S5). We noticed in Figure 3b that for all the devices the response at low concentrations below 1 ng/mL is negligible whereas at concentrations above 1 ng/mL, the devices show a significant change in conductance even for a slight increase in concentration. To exploit the wide detection range and selectivity of the device, it was applied to detect phosphate in complex Hoagland fertilizer solutions, typically containing 45 µg/mL to 310 µg/mL of phosphate alongside other anions (e.g., sulfates, nitrates) in a 15% to 100% fertilizer solution, respectively [Table S1 and S2]. The measured Hoagland concentration signal range of 1.01-0.94 V across three devices (D1, D2, D3) closely aligned with the ideal phosphate solution range of 1.11-1 V (Grey region, Figure 3b), despite minor deviations suggested due to pH interference, the presence of other anions and higher acidity of the base solution compared to the standard phosphate solution.
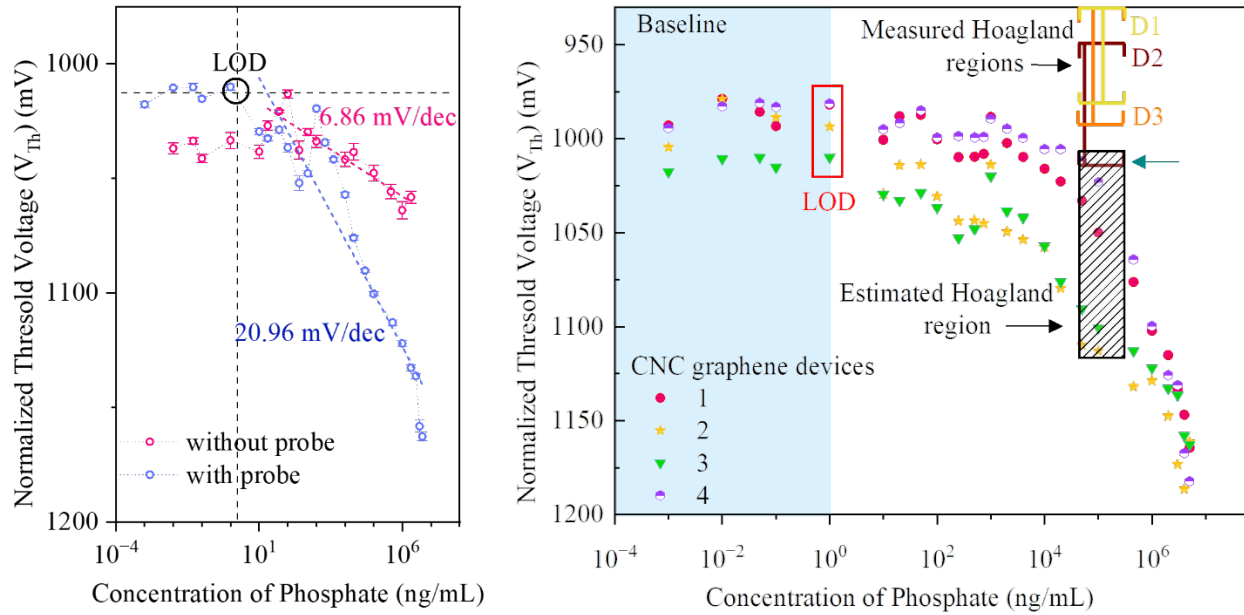
Figure 3: a) Comparative responses of bio-based ferritin functionalized (blue dots) and non-ferritin functionalized (red dots) graphene ink devices to phosphate solutions of different concentrations (1 pg/mL – 5 mg/mL); b) Response trend of the four ferritin functionalized bio-based graphene ink devices to phosphate solutions (1 pg/mL – 5 mg/mL) and to Hoagland fertilizer solutions (45 µg/mL – 310 µg/mL); indicated as D1, D2 and D3.

Traditional FET-based analyte sensors calculate the LOD and sensitivity from threshold voltage (V_{Th}) in transfer curve data.[29] In our system, we measured 50 data cycles for each concentration over 250 seconds, averaging the response to represent the sensor's behavior. However, this approach can obscure key factors such as analyte reaction rate, stabilization, and matrix effects, especially at lower concentrations where the calibration curve's linearity diminishes, limiting accurate LOD prediction. We applied a more advanced CNN model to overcome these challenges and capture the non-linearity at low concentrations. CNN multi-layered neural networks are well-suited for processing complex, non-linear data traits, revealing hidden patterns, and improving kinetic analysis by leveraging the locality of the sequential data with minimized model complexity.[37] [38] Specifically, the DL model aims to (i) identify the optimized

response window from concentration-specific kinetic data automatically with a data-driven method, and (ii) predict the true phosphate concentration in unknown fertilizer solutions.[21]

Initially, from V_{Th} measurements we observed consistent device behavior up to 35 cycles, with increased irregularity between cycles 35-50 (Figure S6). Applying the DL model only to the V_{Th} values over the first 35 cycles resulted in high CV and low r^2 values [Table S3]. We then allow the model to encompass the kinetic signals representing all 50 cycles and convert them into concentration-specific heatmaps (Figure S7a). To mitigate device fluctuations, we subtracted the heatmaps from the DI water phase (Figure S7b) and applied a robust scaler to strengthen the kinetic signal and reduce outliers.[39] The DL model processes the data through a convolutional structure that is effective in capturing local structures, pooling layers that improve the generalizability of the model, and three densely connected layers. With the preprocessing procedure converting the sum of 50-cycle transfer curves (Figure 4a i) into a 2D heatmap (Figure 4a ii), the DL model effectively captures target-specific information such as reaction rate, drift, pH response, and V_{Th} change. The model allows us to combine information from different formats and learn the intrinsic complex physics with minimal model complexity. The neural network uses 1D convolution (1×2 kernel) for V_{Th} data and 2D convolution (2×2 kernel) for transfer curves, converting 50-cycle measurements into heatmaps. After max pooling, the CNN method reduces each input to two nodes. The final two-layer artificial neural network (ANN) concatenates these predecessor outputs to generate the predicted values, as detailed in Figure S8. By further optimizing the gate voltage window (0-2V) and time window (82-165 s) (Figure 4a ii), we achieved a low CV and a high r^2 when comparing predicted phosphate concentrations with validation data [Table S3].

This combined approach, utilizing both V_{Th} dynamics and kinetic signals, resulted in an r^2 of 0.951 (Figure 4b i), a CV of 1.51% of the obtained r^2 values [Table S3], and a CV of 6%

considering the concentration predictions of all devices (Figure S9). We conducted an ablation study to assess the impact of our model choice by replacing it with a multivariate linear regressor. This substitution resulted in a performance drop, with the r^2 score decreasing from 0.951 to 0.892 (Figure S10). These findings highlight the advantage of our model design to a conventional multivariate linear regressor.

Finally, we applied the model to predict phosphate concentrations in Hoagland fertilizer solutions commonly used in aeroponic systems, achieving a CV value of concentrations below 5.39% in blind tests on four samples (Figure 4b ii), confirming the sensor's high predictive accuracy for unknown Hoagland concentrations.

a) (i)   Transfer curve (1D plot)

(ii)   Heatmap (2D Plot)

b) (i)   r² = 0.951

(ii)
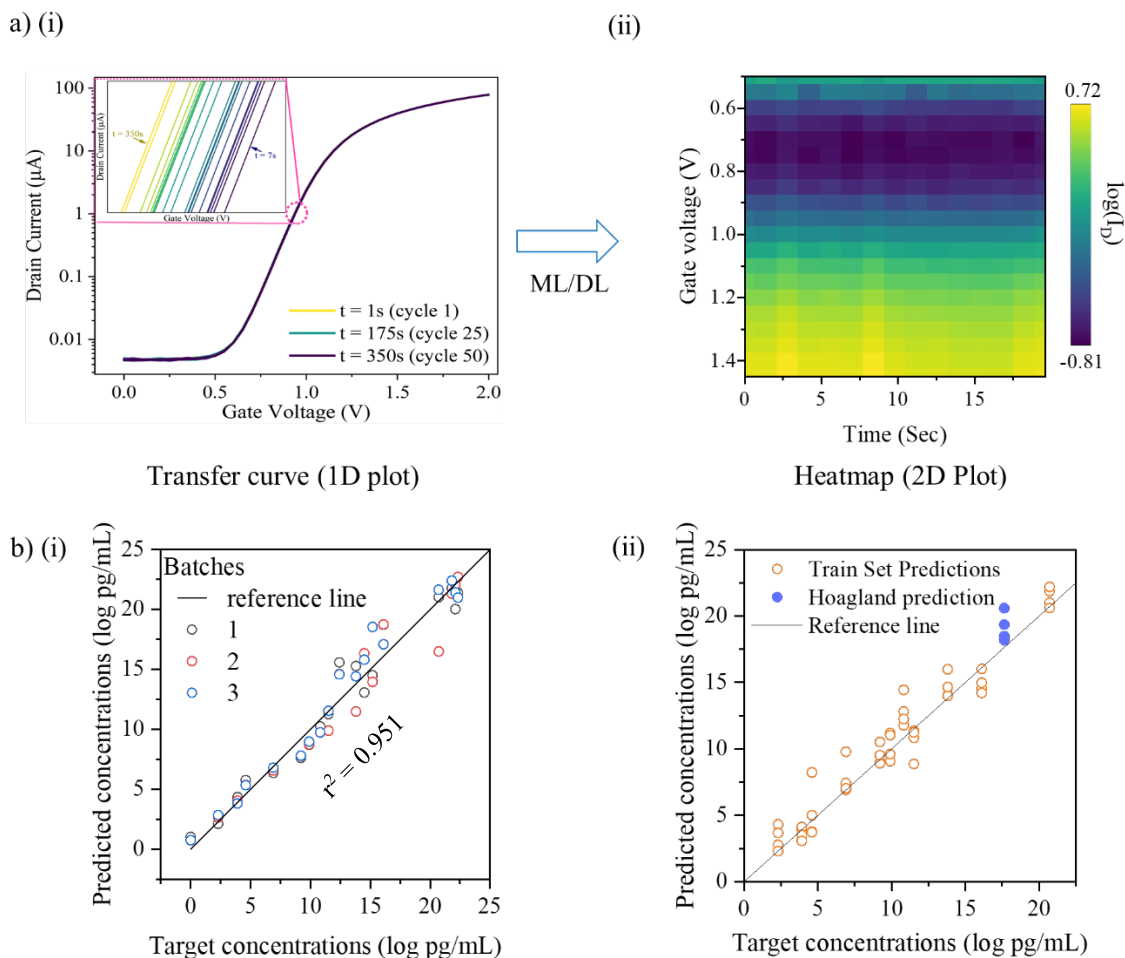
Figure 4: a) (i) Schematic of the 50 cycles transfer curve that changes over different stages of the analyte reaction with the sensor probe and (ii) the conversion of the kinetic data to 2D heatmap after DI water data calibration and optimal window selection [Concentration: 1µg/mL]; b) (i) Model predictions on the validation dataset composed of 57 phosphate samples from 3 different batches for the model with optimal V_G and time subsets and (ii) Final model predictions on the blind testing dataset of Hoagland fertilizer solutions.

To leverage the sensitivity of our sensor toward phosphate ions, we integrated the sensor chips into a handheld prototype system for real-time monitoring. This handheld sensing system is designed for remote use, eliminating the need for complex benchtop setups. At the core of the system is a disposable sensor platform connected to a portable readout device. The sensor employs an N-channel depletion-mode MOSFET, with the gate terminal connected to a ferritin-functionalized biobased graphene film, allowing for direct interaction with the target analyte solution. When the target solution is applied to the functionalized graphene surface, it alters the gate potential. The microcontroller unit (MCU) controls a digital-to-analog converter (DAC) module, generating the necessary gate bias. The sensor signal at the gate terminal is converted into the output voltage (V_d). Following signal amplification via an operational amplifier (OpAmp), an analog-to-digital converter (ADC) digitizes the analog signal. This output signal is then processed by the 'coolterm' software on a laptop or smartphone, facilitating easy data transfer to an accessible platform. The circuit diagram is shown in Figure S11a and the prototype is shown in Figure S11b.

For sensitivity testing, different concentrations of phosphate solutions, ranging up to 5 mg/mL, were sequentially applied to the sensor chip and measured continuously for 10 minutes per concentration. The attached probe captures phosphate ions from the analyte solution, generating an output voltage (V_d) that decreases as phosphate ion concentration increases (Figure 5a). The negative charge of phosphate ions at the gate terminal repels electrons in the n-type channel. As ion concentration rises, the depletion of electrons increases, resulting in reduced

15

conductivity. This behavior is consistent with the results obtained from the semiconductor analyzer setup shown in Figure 3a, where the threshold voltage increases with increasing phosphate concentrations, indicating that more voltage is required to activate the FET due to decreased channel conductance.

To evaluate the sensor's performance in the presence of common interfering ions found in fertilizers, such as chloride (Cl^-), sulfate (SO_4^{2-}), and bicarbonate (HCO_3^-), we tested analyte solutions at similar concentrations (1 µg/mL or 1 ppm) sequentially. The sensor demonstrated a significantly higher sensitivity toward phosphate ions compared to other anions, as illustrated in Figure 5b. This finding suggests that ferritin effectively captures HPO_4^{2-} ions even in a mixed ionic environment. We quantified our observations by calculating the selectivity coefficient (K_{ij}; where i = target ion, j = interfering ion) for each analyte solution [detailed calculations are provided in the supplementary materials]. The results showed Kij << 1 for all interfering ions, confirming the sensor's high selectivity toward HPO_4^{2-} ions.

The observed selectivity can be attributed to two main factors: (a) Coulombic interactions and (b) Lewis acid-base interactions of HPO_4^{2-} with the hydrated iron oxide core of ferritin.[40] These synergistic effects enhance the sensor chip's ability to capture HPO_4^{2-} ions, highlighting its efficacy in real-world applications.
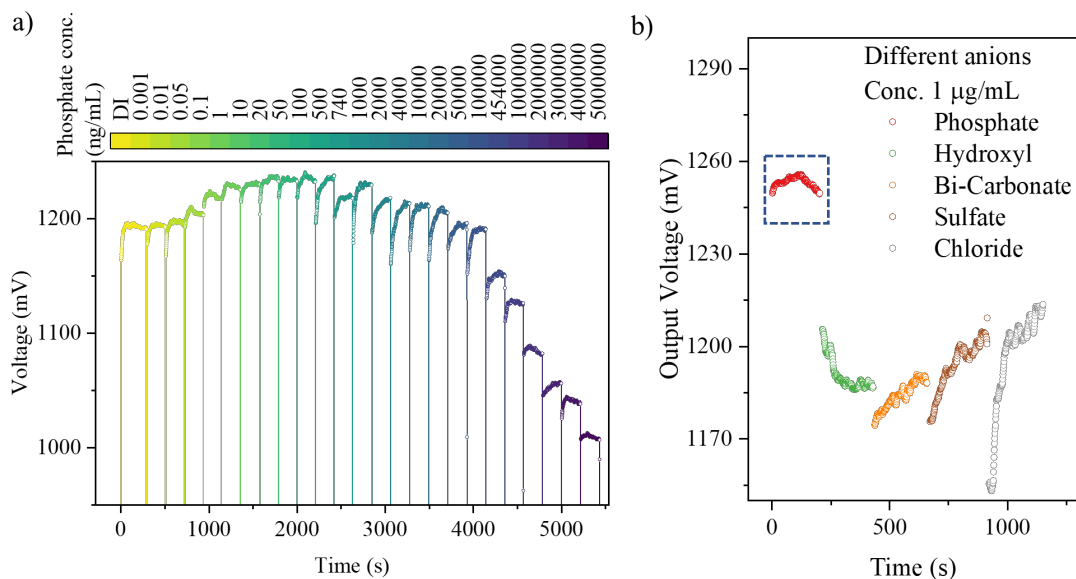
Figure 5: a) Real-time measurements of phosphate solutions at different concentrations (DI, 1 pg/mL-5 mg/mL) and b) Selectivity measurement of different anion solutions of a given concentration (1 µg/mL) with a handheld prototype setup where the ferritin functionalized bio-based graphene device acts as a sensing element. The blue dotted box highlights the response to phosphate ions.

3. Conclusion

In this work, the seamless integration of plant-based materials into FET sensor fabrication to monitor plant growth conditions in aeroponic systems supports our approach toward sustainability and recyclability. Our biobased graphene phosphate sensing device is capable of detecting the concentrations from 1 ng/mL (1 ppb) to 3 mg/mL (3,000 ppm) level with a sensitivity of 14.1 mV/dec after pH correction. This vast range of detection capabilities is ideal for monitoring phosphate levels in fertilizer solutions as well as in drinking water and wastewater. We integrated the remote gate FET sensor technology with DL methodology, which helps to reduce the device non-uniformity and pH interference effects, helps capture the response to lower analyte concentrations, and eliminates other complexities of FET measurements. This synergistic approach results in a reduced CV< 5% and achieves a high r^2 value of 0.95. As a proof-of-concept,

17

we employed Hoagland fertilizer solution to our device to quantify the phosphate concentration, which results in a good precision of CV=5.4%. Our work provides a sustainable approach to nutrient sensing in the plant growth facilities and has the potential to produce real-time sensing devices featuring a low cost and ease of use.

4. Experimental Section

Graphene ink synthesis: Graphene-CNC ink was produced by a plant-derived graphite synthesis and liquid phase exfoliation process as described in previous work.[26] [27] Briefly, carboxylated cellulose nanocrystals isolated from Miscanthus x giganteus were dispersed in water (2 mg/mL) with 5 min of probe sonication. The plant-based graphite was prepared by ball milling hardwood biochar with iron powder (<10µm, Sigma Aldrich) and heating to 1,200 °C for 1 hour followed by a slow cooling step to 1,100 °C over 4 hrs, at which point it was then cooled to room temperature. The resulting powder was washed with 1 M sulfuric acid followed by DI water until neutral, and vacuum oven-dried at 120 °C overnight. This bio-derived graphite powder was directly added (50 mg/mL) to an aqueous CNC dispersion (2 mg/mL) and probe-sonicated for 10 hrs to shear into graphene nanoplatelets in solution. The solution was then centrifuged to remove non-exfoliated material at 3,700 g for 30 min. The resulting supernatant was concentrated by rotary evaporation to a concentration of 15 mg/mL, and cyrene was added (25%/v) to increase the viscosity of the resulting ink. The ink was sonicated and filtered through a 0.7 µm syringe filter to remove any potential aggregates before drop-casting.

The ink was drop-casted on the Si/SiO$_2$ surface which acts as a sensing chip in a remote gate FET setup and annealed for half an hour at 600 °C under 50 sccm nitrogen flow. Before ferritin

protein attachment, the inked surface was immersed in a linker solution (1-pyrenebutyric acid N-hydroxysuccinimide ester/$C_{24}H_{19}NO_4$ in 1:10 ratio in N, N-dimethylformamide solvent) for 2 hrs to initiate pyrene-graphitic interaction. This step enhances the stability of the anchored protein on the sensor surface. In the next step, ferritin (Sigma-Aldrich, ferritin from horse spleen) was anchored on the sensor surface through NHS coupling by incubating the sensor device in the ferritin solution (10 mg mL^{-1} in DI water) for 2-4 hours. After incubation, the surface was thoroughly washed with DI water several times and prepared for the FET measurement.

Electrical measurements: In transfer curve measurement, a fixed V_{ds} (0.05 V) was applied and the gate potential V_G was swept from 0 to 2.0 V. Threshold voltage (V_{Th}) refers to the gate voltage corresponding to 1 μA drain current (I_{ds}) in transfer curve measurement. During phosphate sensing measurements, the dynamic response of the sensor was recorded by measuring the I_{ds} change after exposing it to different ion concentrations. The transfer curve measurement for each concentration has been repeated up to 50 cycles for 250 seconds. Sodium phosphate dibasic (Na_2HPO_4) was used as the source of phosphate ions in our experiment and is dissolved in DI water.

Machine learning toolkits: The DL model was implemented using the Keras API with a TensorFlow backend, and further supported by machine learning tools - including scikit-learn for cross-validation and matplotlib for visualization.[41] [42] [43] This DL integration ensures a robust and scalable pipeline for our experiment.

Associated content

Supporting information

Ferritin functionalized bio-based graphene ink drop-casted device fabrication; AFM image of the bio-based graphene ink; I_D/I_G ratio analysis of the Raman spectra of bio-based graphene ink at different annealing temperatures; pH sensitivity curve of the fabricated device; LOD calculation and CV value analysis of the device response; Component description of Hoagland fertilizer solutions; V_{Th} vs Concentration curves (50 cycles); Heatmaps of the transfer curve after calibration; DL visualization schematic, CV value analysis of concentration prediction using DL model; Ablation study of the model prediction on the validation data sets composed of phosphate solution samples and blind test of fertilizer solution samples; Comparative study of r^2 and CV values obtained from deep learning and linear regression models; Description of handheld device set-up; Selectivity analysis of the fabricated device.

Author Contributions

R. Ghosh, H. J. Jang, and J. Chen conceptualized and conceived the idea of the project. Electrical measurements, device fabrication, and interpretation of data were carried out by R. Ghosh. Computational analysis was carried out by F. Zhang and Y. Chen. The graphene ink was prepared by J. Hui and M. C. Hersam. The CNC and graphite from biochar were prepared by H. You and S. J. Rowan. K. Vittore, D. K. Lee, and E. A. Ainsworth did the Miscanthus farming and Hoagland fertilizer preparation. The XPS measurement was done by R. Vepa and J. W. Elam and analyzed by R. Ghosh. Functionalized samples were prepared by R. Ghosh and W. Zhuang suggested the process. R. Ghosh, H. J. Jang, X. Huang, and H. Pu participated in designing the experiments. All authors contributed in preparing the manuscript. J. Chen supervised the project.

Declaration of interests

The authors declare no competing financial interest.

Data Availability

The data that support the findings of this study are available from the corresponding author J. Chen upon reasonable request.

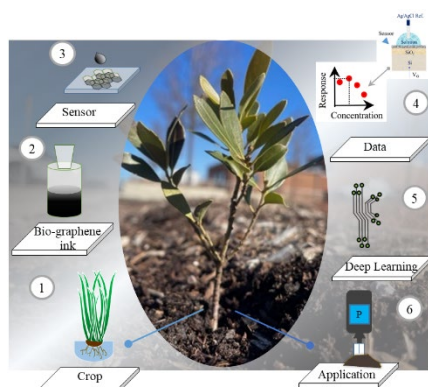**References:**

[1]   L. F. Møller, H. U. Riisgård, *Journal of Experimental Marine Biology and Ecology* **2007**, *351*, 92-105.

[2]   N. N. Rabalais, R. E. Turner, *Limnology and Oceanography Bulletin* **2019**, *28*, 117-124.

[3]   A. Frolova, M. P. Miglietta, *Frontiers in Marine Science* **2020**, *7*.

[4]   A. J. Kollar, *Environmental Progress & Sustainable Energy* **2023**, *42*, e14069.

[5]   R. D. Sabo, C. M. Clark, D. A. Gibbs, G. S. Metson, M. J. Todd, S. D. LeDuc, D. Greiner, M. M. Fry, R. Polinsky, Q. Yang, H. Tian, J. E. Compton, *Journal of Geophysical Research: Biogeosciences* **2021**, *126*, e2020JG005684.

[6]   J. Garzón, L. Montes, J. Garzón, G. Lampropoulos, *Agronomy* **2023**, *13*, 2517.

[7]   F. Khan, A. B. Siddique, S. Shabala, M. Zhou, C. Zhao, *Plants* **2023**, *12*, 2861.

[8]   aX. Zhao, Y. Lyu, K. Jin, H. Lambers, J. Shen, *Frontiers in Plant Science* **2021**, *11*; bK. J. Walters, B. K. Behe, C. J. Currey, R. G. Lopez, *HortScience horts* **2020**, *55*, 758-767.

[9]   S. Yin, L. Dong, *Advanced Materials Technologies* **2024**, *9*, 2302073.

[10]   P. Rosario, R. Viswash, T. Seenivasan, S. Ramalingam, K. L. Sellgren, S. Grego, L. Trotochaud, *Environmental Health Insights* **2021**, *15*, 11786302211019218.

[11]   N. K. Ibnul, C. P. Tripp, *Talanta* **2022**, *238*, 123043.

[12]   H. Yi, S. Hu, Y. Zhang, X. Wang, Z. Xia, Y. Lei, M. Duan, *Agriculture* **2023**, *13*, 884.

[13]   Q.-L. Li, N. Bao, S.-N. Ding, *Electroanalysis* **2014**, *26*, 2710-2715.

[14]   M. R. Ganjali, P. Norouzi, M. Ghomi, M. Salavati-Niasari, *Analytica Chimica Acta* **2006**, *567*, 196-201.

[15]   W.-L. Cheng, J.-W. Sue, W.-C. Chen, J.-L. Chang, J.-M. Zen, *Analytical Chemistry* **2010**, *82*, 1157-1161.

[16]   V. Patel, P. Kruse, P. R. Selvaganapathy, *Journal of The Electrochemical Society* **2022**, *169*, 077505.

[17]   S. V. Mapare, P. L. Yu, A. Sarkar, S. C. Mukhopadhyay, in *2013 Seventh International Conference on Sensing Technology (ICST)*, **2013**, pp. 411-418.

[18]   K. S. Bhat, R. Ahmad, T. Mahmoudi, Y.-B. Hahn, *Chemical Engineering Journal* **2021**, *417*, 128064.

[19]   S. Mao, H. Pu, J. Chang, X. Sui, G. Zhou, R. Ren, Y. Chen, J. Chen, *Environmental Science: Nano* **2017**, *4*, 856-863.

[20]   T. Ono, S. Okuda, S. Ushiba, Y. Kanai, K. Matsumoto, *Materials* **2024**, *17*, 333.

[21]   H.-J. Jang, H.-A. Joung, A. Goncharov, A. G. Kanegusuku, C. W. Chan, K.-T. J. Yeo, W. Zhuang, A. Ozcan, J. Chen, *ACS Nano* **2024**, *18*, 24792-24802.

[22]   J. Zhang, P. Srivatsa, F. H. Ahmadzai, Y. Liu, X. Song, A. Karpatne, Z. J. Kong, B. N. Johnson, *Biosens Bioelectron* **2024**, *246*, 115829.

[23]   K. S. Desale, S. V. Shinde, *Expert Systems* **2023**, *40*, e13394.

[24]   A. V. Babu, T. Zhou, S. Kandel, T. Bicer, Z. Liu, W. Judge, D. J. Ching, Y. Jiang, S. Veseli, S. Henke, R. Chard, Y. Yao, E. Sirazitdinova, G. Gupta, M. V. Holt, I. T. Foster, A. Miceli, M. J. Cherukara, *Nature Communications* **2023**, *14*, 7059.

[25]   Y. LeCun, Y. Bengio, G. Hinton, *Nature* **2015**, *521*, 436-444.

[26]   H. You, J. Hui, Y. Zhou, K. Vittore, J. Zhang, L. E. Chaney, S. Chinta, Y. Zhao, G. Lim, D. Lee, E. A. Ainsworth, J. B. Dunn, V. P. Dravid, M. C. Hersam, S. J. Rowan, *Small* **2024**, *20*, 2406669.

[27]   J. Hui, H. You, A. Van Beek, J. Zhang, A. Elahi, J. R. Downing, L. E. Chaney, D. Lee, E. A. Ainsworth, S. Chaudhuri, J. B. Dunn, W. Chen, S. J. Rowan, M. C. Hersam, *ACS Applied Materials & Interfaces* **2024**, *16*, 57534-57543.

[28]   T. Carey, A. Alhourani, R. Tian, S. Seyedin, A. Arbab, J. Maughan, L. Šiller, D. Horvath, A. Kelly, H. Kaur, E. Caffrey, J. M. Kim, H. R. Hagland, J. N. Coleman, *npj 2D Materials and Applications* **2022**, *6*, 3.

[29]   H.-J. Jang, X. Sui, W. Zhuang, X. Huang, M. Chen, X. Cai, Y. Wang, B. Ryu, H. Pu, N. Ankenbruck, K. Beavis, J. Huang, J. Chen, *ACS Applied Materials & Interfaces* **2022**, *14*, 24187-24196.

[30]   A. C. Ferrari, D. M. Basko, *Nature Nanotechnology* **2013**, *8*, 235-246.

[31]   T. Palaniselvam, H. B. Aiyappa, S. Kurungot, *Journal of Materials Chemistry* **2012**, *22*, 23799-23805.

[32]   A. Eckmann, A. Felten, A. Mishchenko, L. Britnell, R. Krupke, K. S. Novoselov, C. Casiraghi, *Nano Letters* **2012**, *12*, 3925-3930.

[33]   R. Y. N. Gengler, D. S. Badali, D. Zhang, K. Dimos, K. Spyrou, D. Gournis, R. J. D. Miller, *Nature Communications* **2013**, *4*, 2560.

[34]   Y. Zhang, C. Liu, W. Shi, Z. Wang, L. Dai, X. Zhang, *Langmuir* **2007**, *23*, 7911-7915.

[35]   V. Mishyn, A. Hugo, T. Rodrigues, P. Aspermair, H. Happy, L. Marques, C. Hurot, R. Othmen, V. Bouchiat, R. Boukherroub, W. Knoll, S. Szunerits, *Sensors & Diagnostics* **2022**, *1*, 235-244.

[36]   G. Zhou, B. Jin, Y. Wang, Q. Dong, A. Maity, J. Chang, R. Ren, H. Pu, X. Sui, S. Mao, J. Chen, *Molecular Systems Design & Engineering* **2020**, *5*, 936-942.

[37]   S. Kiranyaz, O. Avci, O. Abdeljaber, T. Ince, M. Gabbouj, D. J. Inman, *Mechanical Systems and Signal Processing* **2021**, *151*, 107398.

[38]   H. Sajindra, T. Abekoon, J. A. D. C. A. Jayakody, U. Rathnayake, *Smart Agricultural Technology* **2024**, *7*, 100395.

[39]   M. M. Ahsan, M. A. P. Mahmud, P. K. Saha, K. D. Gupta, Z. Siddique, *Technologies* **2021**, *9*, 52.

[40]   J. C. Mendez, T. Hiemstra, *ACS Earth and Space Chemistry* **2019**, *3*, 129-141.

[41]   A. Gulli, S. Pal, *Deep learning with Keras*, Packt Publishing Ltd, **2017**.

[42]   F. Pedregosa, G. Varoquaux, A. Gramfort, V. Michel, B. Thirion, O. Grisel, M. Blondel, P. Prettenhofer, R. Weiss, V. Dubourg, *the Journal of machine Learning research* **2011**, *12*, 2825-2830.

[43]   J. D. Hunter, *Computing in science & engineering* **2007**, *9*, 90-95.

Table of Content

Accurate, real-time nutrient monitoring is challenging in precision agriculture due to cost and technical limitations. Aligned with a circular green economy, a deep learning-integrated remote-gate FET sensor with plant-derived graphene electrodes offers a sustainable solution. Functionalized with phosphate-binding ferritin, it provides high sensitivity, low variation, and a 1 ng/mL (1 ppb) detection limit for scalable, on-site phosphate sensing.

Real-Time Phosphate Monitoring via Plant-derived Graphene Ink FET Sensors Integrated with Deep Learning

Rapti Ghosh,[1,2] Fengxue Zhang,[3] Hyun-June Jang,[1,2] Janan Hui,[4] Kayla Vittore,[5] Haoyang You,[6] Rozyyev Vepa,[7] Wen Zhuang,[1,2] Xingkang Huang,[1,2] Haihui Pu,[1,2] Jeffrey W. Elam,[7] Stuart J. Rowan,[1,2,6] DoKyoung Lee,[5] Elizabeth A. Ainsworth,[5,8] Mark C. Hersam,[4,9] Yuxin Chen,[3] Junhong Chen[1,2]*

[1]Pritzker School of Molecular Engineering, University of Chicago, Chicago, IL 60637, USA

[2]Chemical Sciences and Engineering Division, Physical Sciences and Engineering Directorate, Argonne National Laboratory, Lemont, IL 60439, USA

[3] Department of Computer Science, University of Chicago, Chicago, IL 60637, USA

[4] Department of Chemistry, Northwestern University, Evanston, Illinois 60208, USA

[5] Department of Crop Sciences, University of Illinois Urbana−Champaign, Urbana, Illinois 61801, USA

[6] Department of Chemistry, University of Chicago, Chicago, Illinois 60637 United States

[7] Applied Materials Division, Argonne National Laboratory, Lemont, IL, 60439, USA

[8] Department of Plant Biology, University of Illinois Urbana Champaign, Urbana, Illinois 61801, USA

[9] Department of Materials Science and Engineering, Northwestern University, Evanston, Illinois 60208, USA

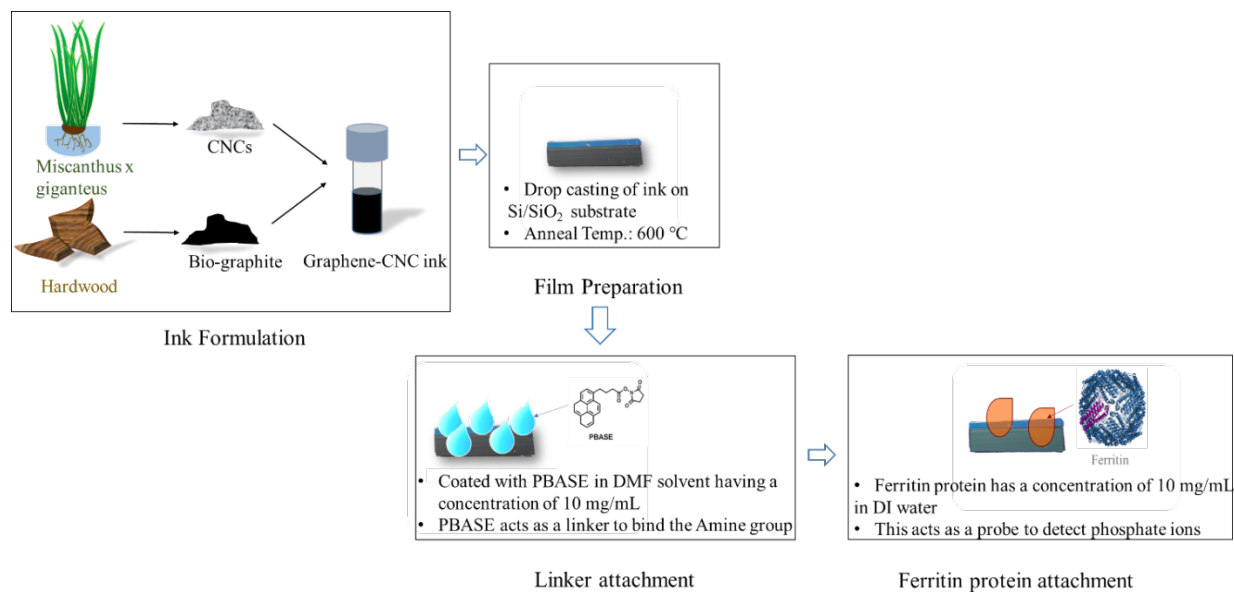*Corresponding author: Junhong Chen: junhongchen@uchicago.edu

Figure S1: Schematic diagram of ferritin functionalized bio-based graphene ink drop-casted device preparation.
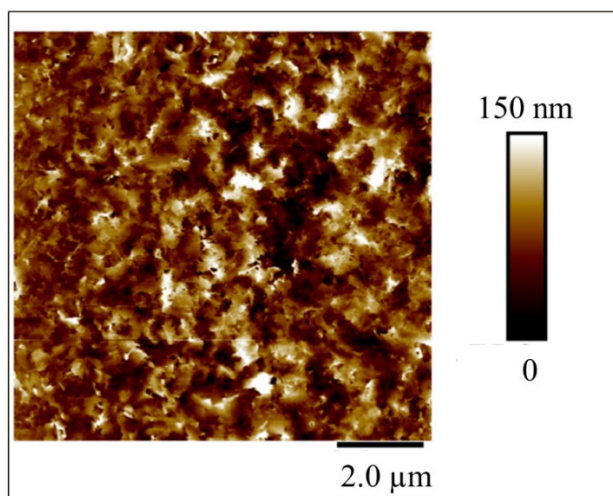

Figure S2: AFM image showing the surface topography of the film prepared by casting the bio-based graphene ink on a Si/SiO_2 substrate.
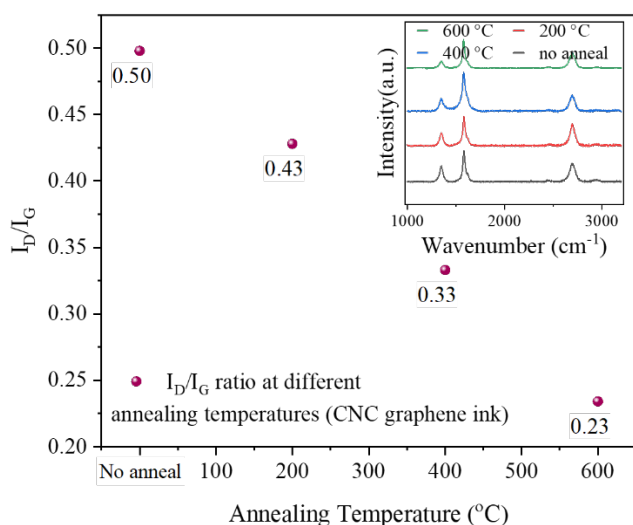
Figure S3: Comparative analysis of I_D/I_G ratio of bio-based graphene ink annealed at different temperatures; Inset: Raman spectra of the ink at corresponding annealing temperatures.
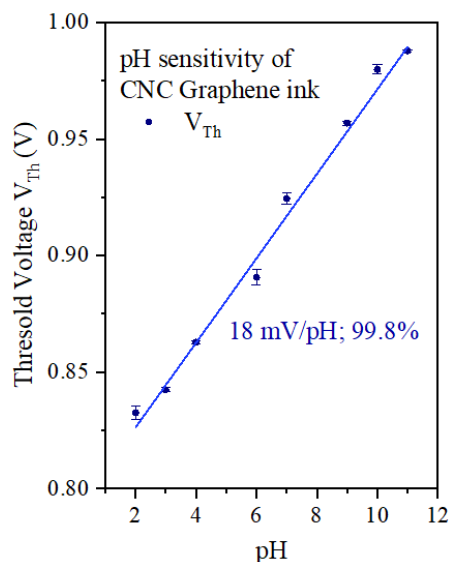
Figure S4: pH sensitivity of the ferritinized bio-based graphene device.

- Calculation of sensitivity:

The LOD is calculated using the formula (3 * standard deviation of the blank)/sensitivity [1]

In Figure 3a, the linear slope of the calibration curve (with probe) is 20.96 mV/dec which indicates the sensitivity of the device including the phosphate effect and the pH effect. The linear slope of the calibration curve (without probe) is 6.86 mV/dec which indicates the sensitivity of the

controlled device considering only the pH effect. So the resultant sensitivity considering only phosphate response is (20.96-6.86) =14.1 mV/dec.

The standard deviation of the blank is 0.005.

So the limit of detection is LOD = (3 * standard deviation of the blank)/sensitivity

$$= [(3 * 0.005)/0.01410] \text{ ng/mL}$$

$$= 1 \text{ ng/mL}$$

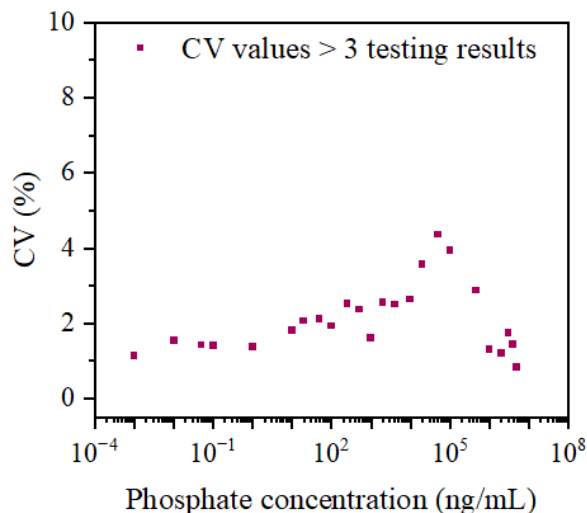Figure S5: CV values of responses at different phosphate concentrations between different devices.

Table S1: Components of Hoagland fertilizer solution in 100% P

100% P Recipe pH = 4.5	Salts dissolved into 1 L of DI water
2M KNO$_3$	6.06g
2M Ca(NO$_3$)$_2$•4H$_2$O	9.44g
2M MgSO$_4$•7H$_2$O	4.93g
1M NH$_4$H$_2$PO$_4$	1.15g

Table S2: Components of Hoagland fertilizer solution in 15% P

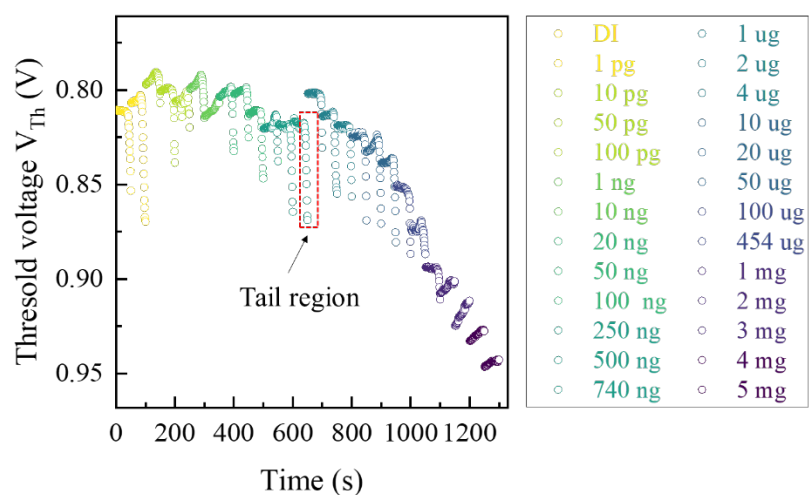| 15% P Recipe pH = 5.8	Salts dissolved into 1 L of DI water
2M KNO$_3$	6.06g
2M Ca(NO$_3$)$_2$•4H$_2$O	9.44g
2M MgSO$_4$•7H$_2$O	4.93g
1M NH$_4$H$_2$PO$_4$	0.17g
Urea	0.51g

Figure S6: V_{Th} vs. concentration curve of 50 cycles data for concentrations ranging from 1 pg/mL to 5 mg/mL.
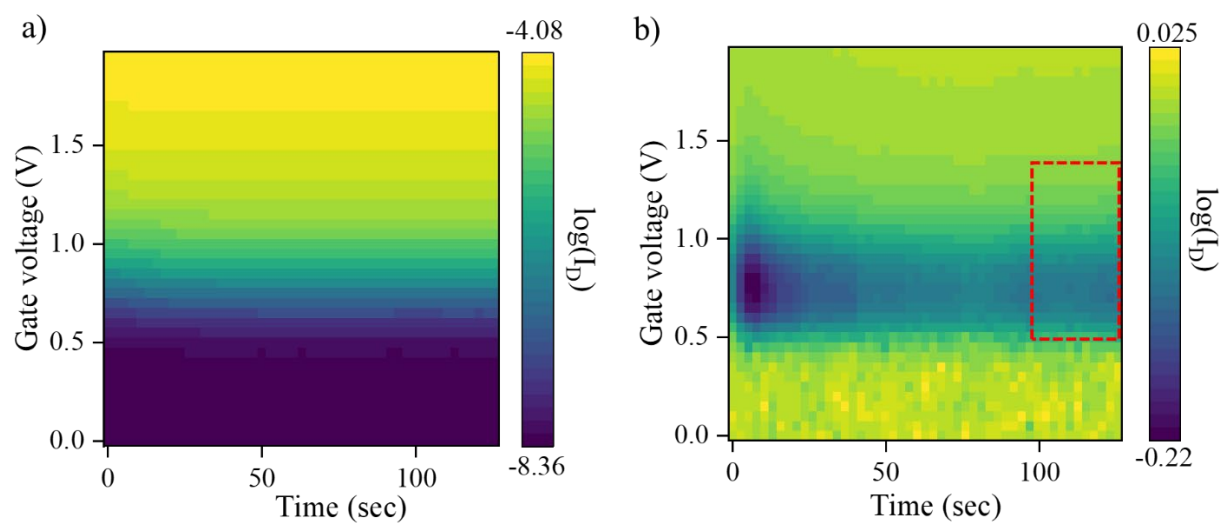

Figure S7: a) Heatmap of the raw transfer curve of 50 cycles from the entire operation range, b) Heatmap after DI water calibration. [Concentration: 1 µg/mL]
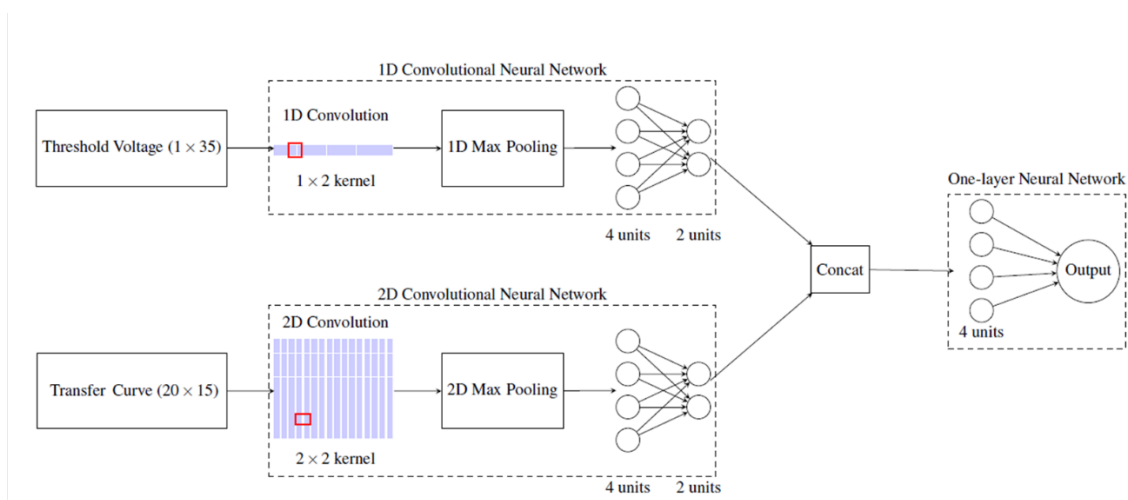
a)

Figure S8: a) The visualization of 1D CNN, 2D CNN, and two-layer ANN with integrated sliding windows.
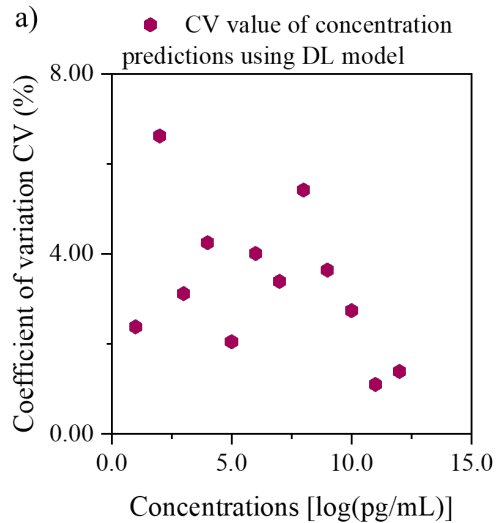
a)

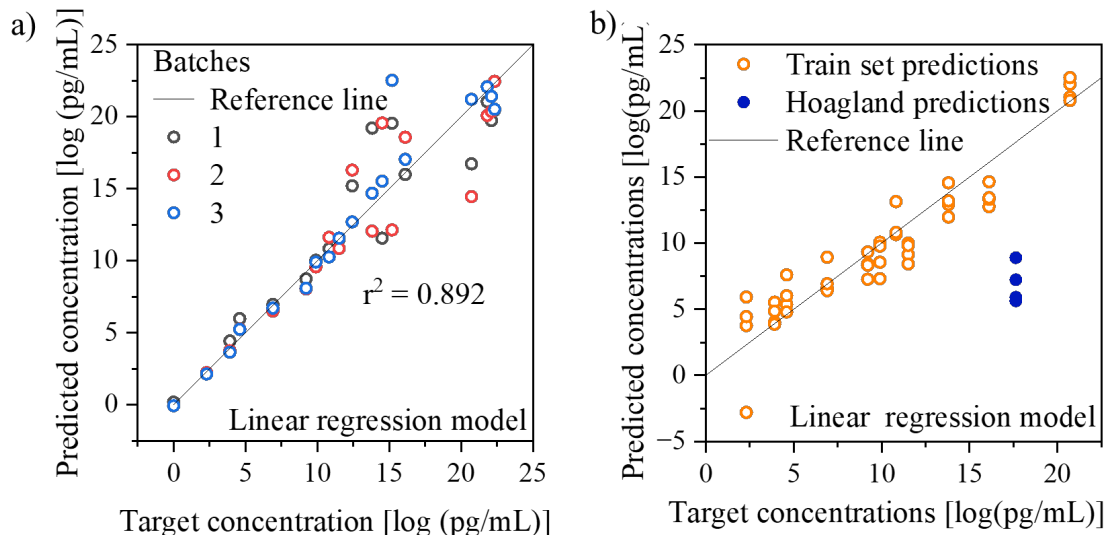Figure S9: CV values of concentration predictions using an optimized DL model.

Figure S10: a) Ablation study of the model predictions on the validation dataset composed of 57 phosphate samples from 3 different batches for the model with optimal V_G and time subsets and (b) Final model predictions using ablation study on the blind testing dataset of Hoagland fertilizer solution.

Table S3. r^2 and CV values of deep learning models with different input data compared with the traditional linear regression model.

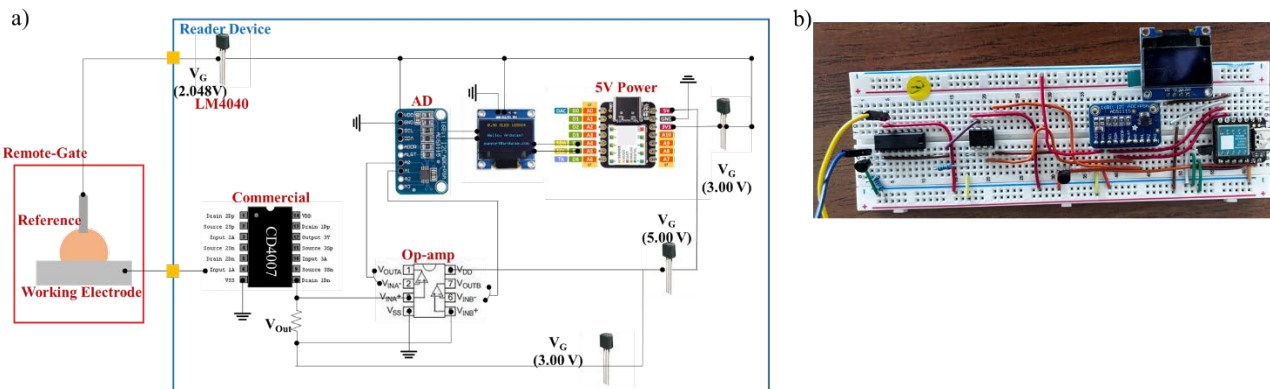| Method		Metric				
		r^2				CV (%) of r^2 values
		Overall	Batch 1	Batch 2	Batch 2	
Deep Learning	Threshold-voltages only	0.845	0.893	0.954	0.688	13.47
	+ Raw transfer curve	0.884	0.877	0.908	0.869	1.90
	+ Device-wise calibration	0.895	0.875	0.919	0.891	2.01
	+ Window selection	**0.951**	**0.970**	**0.935**	**0.947**	**1.51**
Linear Regression	**With all above**	0.892	0.906	0.890	0.881	1.19

Figure S11: a) Circuit diagram and b) real image of the handheld device setup.

- Calculation of selectivity coefficient: (comparing phosphate with chloride)

$$K_{ij} = \frac{10^{\frac{\Delta V}{Sj}} - 1}{10^{\frac{\Delta V}{Si}}}$$

ΔV = change in output voltage ($V_{\text{target ion}} - V_{\text{interfering ion}}$) = (1255-1250) mV = 5 mV

Sj = Nernst slope of interfering ion

Si = Nernst slope of the target ion

59.16 mV/dec for monovalent; 19.72 for trivalent ions.

$$K_{ij} = \frac{10^{\frac{50}{59.16}} - 1}{10^{\frac{50}{19.72}}}$$

$$= 0.12 \ll 1$$

Reference:

[1]   H. A. Molla, R. Bhowmick, A. Katarkar, K. Chaudhuri, S. Gangopadhyay, M. Ali, *Analytical Methods* **2015**, *7*, 5149-5156.